Development and Evaluation of a Backdrivable Vane-Type Rotary Actuator Using Magnetorheological Fluids

Peizhi Zhang , *Student Member, IEEE*, Mitsuhiro Kamezaki , *Member, IEEE*, Kenshiro Otsuki, Shan He, Zhuoyi He , Gonzalo Aguirre Dominguez , *Student Member, IEEE*, and Shigeki Sugano , *Fellow, IEEE*

Abstract—Robot systems with both "intrinsic safety" and "high output" are expected to be implemented in heavy-duty industries such as construction and manufacturing. But there are currently no effective solutions. In our previous work, a backdrivable piston using magnetorheological fluid (MRF) whose viscosity can vary with the applied magnetic field was developed. However, it was a passive device, and its active control scheme was not proposed. The design was complex enough to hinder its implementation to robot arms. In this article, we develop an easily implementable rotary actuator using MRF and propose a basic controller. The actuator was designed based on a vane motor and was driven by hydraulic oil (i.e., MRF), so it can generate high torque. It also has a built-in MRF valve in the vane which can change the output torque and backdrivability with the magnetic field controlled by coil current. Each component was designed to maximize the dynamic range of output torque and backdrivability based on a multiphysics coupling model of electromagnetics, MRF magnetization, and fluid dynamics. Moreover, three basic control modes including backdrivable, high-response, and power-efficiency modes were designed and tested. The experimental results showed that the proposed MRF actuator had both high output and intrinsic backdrivability, and control modes could show the advantages of the MRF actuator.

Index Terms—Functional materials, hydraulic actuators, multiphysics coupling model, prototypes.

I. INTRODUCTION

NOWADAYS, robots that can work safely and effectively in human environments are expected to be implemented in the fields as welfare and live support. These needs accelerate the research on physical human–robot interaction [1], [2]. Such robots must guarantee the safety of surrounding humans or environments and generate a large enough force for the task. For improving safety of robot, many types of compliant actuation systems have been developed to provide backdrivability [3]–[7]. Intrinsic backdrivability is the ability to express the easiness of force transmission from the output axis to the input axis driven by an external force. For humans, when the muscle is relaxed, the limbs can be moved easily by others, which exhibits high intrinsic backdrivability. This flexibility can mitigate possible damage for humans and facilitate interacting objects. For the same reason, human-like high intrinsic backdrivable robots are required for human-centered robots.

Currently, servo systems with electric motors [8] are one of the most widely used compliant actuation systems. They are often applied to lightweight collaborative robots. However, for human-collaborative heavy-duty tasks, such as those in construction and manufacturing, the servo systems are no longer suitable. Actuation systems that can generate a higher force and adaptability to unstructured environments are required. Nevertheless, it is hard to create high backdrivability for contraction and heavy-duty machines, since these machines are often actuated by hydraulic actuator systems and these actuators often own rigid hardware and a narrow bandwidths controller [9]. Many studies attempt rapid control of servo-valves [10] to create compliance. However, it is still hard to fully deal with sudden impacts and collisions [1]. Especially when the controller is not in operation, the hydraulic actuator system without intrinsic backdrivability still causes damage to the surroundings. Thus, it is necessary to develop a hydraulic actuator system with both "intrinsic backdrivability" and "high output" that does not rely on the complex controller.

We thus consider the approach of building intrinsic backdrivability into the hardware and focus on using functional materials, i.e., magnetorheological fluid (MRF) [11]. MRF is an oil that can

TABLE I
COMPARISON OF HUMAN-COOPERATIVE ACTUATORS (*EXPECTED VALUES FOR MRF ACTUATOR)

Actuation system	Electric motor			Fluid power	
Parameters	Harmonic drive [16]	Series elastic actuator [7]	Series clutch actuator [3]	Hydraulic motor [17]	**MRF actuator***
Output torque [Nm]	10^{-5}–10^4 [3] [5] [18]			10^0–10^6 [18]	10^1
Power density [W/kg]	10^2–10^3 [18]			10^2–10^4 [18]	10^2
Durability	Low	Medium	Medium	High	High
Intrinsic backdrivability	Sometimes	Yes (unadjustable)	Yes (adjustable)	No	Yes (adjustable)
Responsivity [ms]	10^1 [16]	10^2 [6]	10^1 [3]	10^2 [19]	10^1
Torque control parameter	Single (Current)		Multiple (motor/clutch current)	Single (relief valve pressure)	Multiple (mganetic field/flowrate)
Dynamic range	Medium	Small	Medium	Medium	Large
Size [mm]	10^2 [16]	Medium (mechanism at arm) [4]	Medium (mechanism at joint)	Large (pump system included)	10^2 (pump system included)
Arrangement	Rigid [4] and felexible connections [26]			Soft connection	Soft connection
Control preciseness	High (no backlash)	Low (due to spring)	Medium	High	Medium
Modeling	Linear			Non-linear	Non-linear

operate under high pressure, making it appropriate to be used as a working fluid in traditional hydraulic actuation systems. MRFs consist of iron particles in an oil suspension. The fluid can transform into a pseudosolid solution with a magnetic field applied, leading to viscosity change. The property of oil and controllable viscosity makes the material suitable for applying in hydraulic systems to achieve high output and intrinsic backdrivability.

Conventionally, devices using MRF are passively driven by the actuator, such as the MRF clutch [12], [13] and MRF damper [14]. The potential of MRFs' oil property, i.e., uncompressible, has not been thoroughly considered, so the devices cannot generate both high output and backdrivability. In response to this, we developed an MRF piston damper that can change the damping force by adjusting the MRF viscosity with a magnetic field [15] and confirmed that it had both high output and backdrivability. However, this is also a passive-driven device, so active-driven devices by MRF are still blank. Thus, with the help of oil property, applying MRF into the hydraulic system to develop an active-driven device that obtained high output and intrinsic backdrivability is our research goal.

In this article, we develop a backdrivable MRF "actuator." We first create a multiphysics coupling model of electromagnetics, MRF magnetization, and fluid dynamics for the MRF actuator to maximize the dynamic range of output torque and backdrivability. Then, we design the built-in MRF valve making the actuator highly integrated to ease manufacturing, assembling, and installation in robot systems. Finally, we design a multivariable controller based on active-drive modeling considering characteristics of flowrate and magnetic field control. In summary, we propose a backdrivable MRF rotary actuator with an easily implementable structure, high output torque, and high backdrivability. As a prototype, we chose a single-vane motor and modified it as an MRF actuator.

II. COMPARISON AMONG ACTUATION SYSTEMS

To clarify features of the MRF actuator, we compare it with existing actuation systems including harmonic drive, series elastic actuator , series clutch actuator (SCA), and hydraulic motor, as listed in Table I. Hydraulic motors possess high power density, harmonic drive contributes high responsiveness, and SCAs hold adjustable torque and backdrivability. As stated above, the MRF actuator uses hydraulic actuation power, so it will have high output, power density [18], and durability. The MRF actuator has
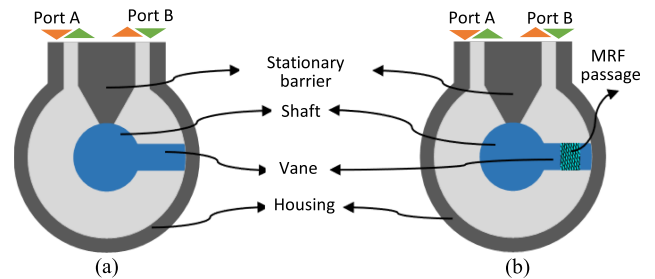

Fig. 1. Schematic diagrams of vane actuators. (a) Normal single vane motor. (b) MRF vane actuator.

the built-in MRF valve, so it also has intrinsic backdrivability and faster responsiveness [20] than those of hydraulic motors [17]. The built-in MRF valve can produce adjustable backdrivability by changing the MRF viscosity, and it is superior to SEAs that cannot change elasticity [7]. The MRF actuator has two manipulated variables, i.e., pump flowrate and magnetic field, so it will provide a wider dynamic range of output torque and backdrivability than those of electric servo systems and hydraulic motors. This multi-input system could offer a variety of control modes. A fluid-based power transmission system may be space-consuming, but it enables more flexible system arrangement, compared with electric motor systems whose power transmission systems are connected by rigid gears and links [4]. However, the built-in MRF valve, nonlinear behaviors of MRF, and multi-input system would cause pressure loss and complicate precise torque control.

In summary, the vane-type MRF actuator with a built-in MRF valve has the potential to provide novel features, including high output torque, intrinsic backdrivability, and faster responsiveness, which can satisfy the requirements of this study. To achieve this, as stated in Section I, we need to design MRF actuator based on a multiphysics coupling model of electromagnetics, MRF magnetization, and fluid dynamics.

III. WORKING PRINCIPLE OF MRF ACTUATOR

1) *Working principle:* As stated in Section I, the MRF actuator is based on a single vane motor due to its simple structure and operation. In the original single vane motor [see Fig. 1(a)], the working fluid flows into the vane motor to generate the pressure difference between the two sides

TABLE II
BASIC SPECIFICATION OF VANE MOTOR

Size (L, H, W)	95, 80, 80 mm
Rotational angle	270°
Shaft diameter	30 mm
Height of vane	14 mm
Length of vane	35 mm
Dry weight	4.3 kg

of the vane. The shaft with the vane rotates to produce a torque. In the MRF actuator [see Fig. 1(b)], the vane has a built-in MRF valve with a narrow passage to allow the MRF to flow between two chambers. By controlling the magnetic field applied to the passage, it can change the MRF viscosity, and then it can change the output torque and backdrivability. As stated in Section II, MRF actuator is a multi-input (pump flowrate and magnetic field) multi-output (torque, speed, and backdrivability) system.

2) *Selection of MRF:* The viscosity of MRF is higher than that of traditional working fluids, i.e., hydraulic oil, which enables the MRF actuator to generate a higher torque. However, backdrivability prefers low-viscosity fluids. Thus, we selected the MRF 122EG from Lord Corporation [21], due to its relatively low initial viscosity.

3) *Target specification:* Table II lists the specifications of the vane motor to be modified. In this preliminary study, we targeted an actuator that could generate more than 15 N·m and has a size of about ϕ100 x 100 mm, which is a specification similar to a human elbow joint.

IV. MECHANICAL DESIGN

We here designed an MRF actuator that could achieve high output torque and high backdrivability.

A. Built-in MRF Valve

Conventional MRF valves do not consider the system size, so they are independently designed and located outside the devices (an MRF valve in [22] is around ϕ100 x 50 mm). MRF actuators will be implemented in robotic systems, e.g., arms and hands, so the MRF valve should be inside the actuator to save space as well as provide rapid and efficient power transmission. Thus, we design a new built-in MRF valve that consolidates the magnetic generator, MRF valve passage, and magnetic flux conductors. The whole structure of MRF vane-type actuator is shown in Fig. 2. Here, we mainly designed the structure of shaft and vane by considering magnetic circuit performance, torque transmission, and ease of assembly.

We designed the magnetic field generator to create magnetic flux in the shaft to save space [see Fig. 3(c)]. The coil was wounded on the shaft core and was covered by the coil cover to prevent both MRF leaking into the shaft and the magnetic field leaking from the core to chambers. The magnetic circuit was formed by the core, magnetic flux conductor, vane, and MRF. For easy assembly and durability, the MRF valve passage was made by the gap between two parts. The gap was stably ensured
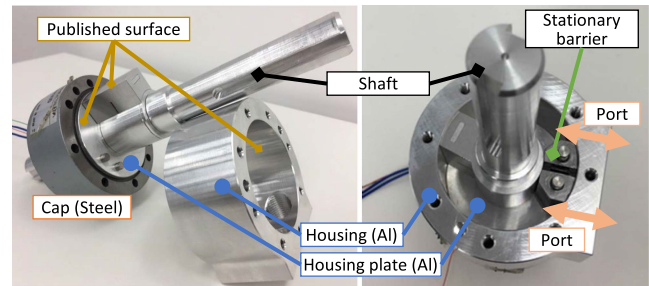
Fig. 2. Structure of MRF vane-type rotary actuator and its surface treatment.
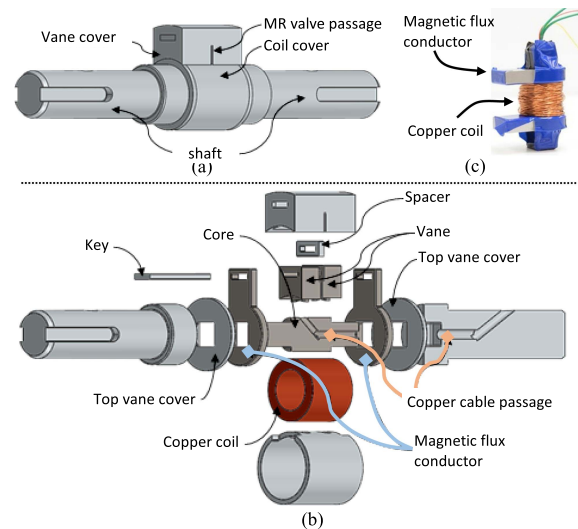
Fig. 3. Designed shaft of MRF actuator including all the reverent parts. (a) Shaft assembly. (b) Components of shaft. (c) Magnetic field generator.

by the spacer [see Fig. 3(b)]. Both vane cover and coil cover were completely seamless to avoid any leakage [see Fig. 3(a)]. We also applied a mortise and tenon structure to simplify the structure, in the connection with the core–shaft, vane–coil cover, and conductor–coil cover.

B. Bi-metal Magnetic Field Generator

Magnetic flux always follows the path of least reluctance, so we adopted a bi-metal structure to effectively make a path (from shaft to vane) for the magnetic flux [23] with a magnetic material (K-M31) and nonmagnetic material (aluminum), as shown in Fig. 4. K-M31 has 2500 μ_0 of the maximum magnetic permeability, 1.25 T of the magnetic saturation, and low hysteresis, which is suitable for the magnetic field generator and conductor. Contrary to this, the permeability of aluminum is the same as that of air, so it can block the leakage of the magnetic field. The red line in Fig. 4 shows the path of the magnetic flux from the core to MRF valve passage. Aluminum to cover the magnetic field generator and conductors will concentrate the magnetic field more on the MRF valve passage. The steel housing was also redesigned using aluminum to avoid magnetic field leakage,
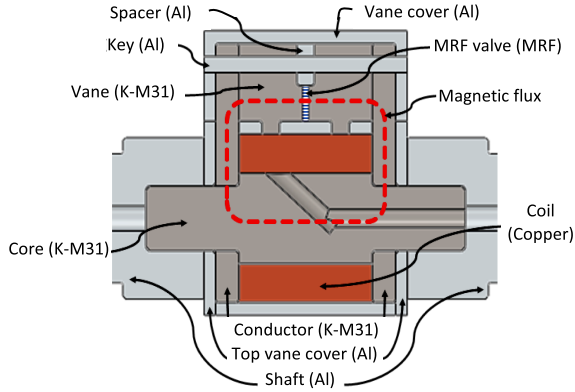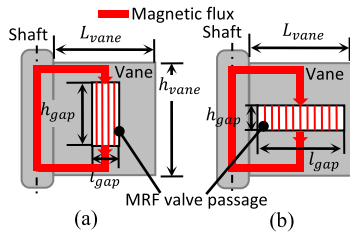
Fig. 4.   Bi-metal magnetic field generator.

Fig. 5.   MRF valve passage configuration. (a) $h_{\text{gap}} > l_{\text{gap}}$. (b) $h_{\text{gap}} < l_{\text{gap}}$.

as shown in Fig. 2. Two additional housing plates were also designed to isolate the chamber from the steel caps.

To determine the parameters of the built-in MRF valve, we here describe the design approach for the built-in MRF valve. All the design parameters should be determined by analyzing their complex relationship. As Table II lists, the base motor was fixed, so the height h_{gap} and width l_{gap} of the passage are the main design parameters. Higher output torque requires a smaller passage area, but this simultaneously degrades backdrivability. Note that different combinations of h_{gap} and l_{gap} that produce the same area can offer different output performance. In $h_{\text{gap}} > l_{\text{gap}}$ [see Fig. 5(a)], the magnetic flux density in the passage largely decreases due to the long magnetic passage, so the MRF viscosity will not change obviously and the dynamic ranges of torque and backdrivability become smaller. In contrast, in $h_{\text{gap}} < l_{\text{gap}}$ [see Fig. 5(b)], the magnetic flux density is more concentrated, so the dynamic ranges of output torque and backdrivability become larger.

As we will explain later, h_{gap} affects the output torque and its dynamic range (see Section V) and the passing area affects the minimum pressure for backdrivable force (see Section VI). We thus decide h_{gap} from output torque requirement and l_{gap} from backdrivability requirement. To achieve this, we iteratively determined them based on a multiphysics modeling and simulation (electromagnetic circuit in Section V) and (MRF magnetization and fluid dynamics in Section VI).

C. Friction Reduction While Maximizing Output Torque

The design of the MRF valve passage could ensure the backdrivability of the MRF actuator. Sealing can mitigate the
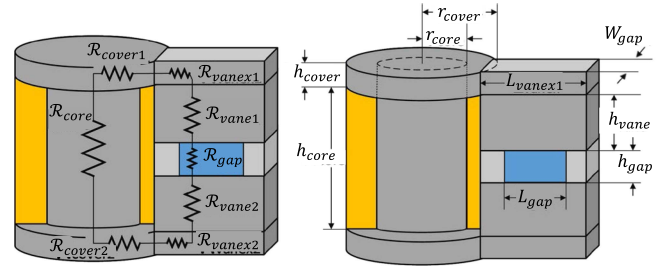

Fig. 6.   Schematic diagram of the magnetic circuit.

leakage of fluid to avoid pressure loss but will bring undesired friction force to degrade backdrivability and low-speed controllability. The aim of this study is to achieve both high output torque and backdrivability, so we adopted pseudosealing with precision machining instead of using the sealing rubber. The gap between the vane and housing was redesigned to only 80 μm and the surface on the housing and vane was machined to $R_a = 0.4$ (see Fig. 2). R_a refers to the average of a set of individual measurements of a surface's peaks and valleys. Smaller R_a represents the smother surface. The thin gap and surface treatment ensured both the minimum leakage (high output-torque) and low initial friction (high backdrivability). We evaluated the effectiveness of this approach using the experimental results.

V. Electromagnetic Circuit Design

We modeled the bimetal magnetic field generator (see Fig. 6) to verify the mechanical design of the built-in MRF valve for magnetic flux conduction. The magnetic flux inside the MRF valve passage can be formulated as follows:

$$\mathcal{F} = NI = \Phi\mathcal{R}, \tag{1}$$

$$B_{\text{gap}} = \Phi / A_{\text{gap}} \tag{2}$$

where $\mathcal{F}$ is the magnetomotive force in ampere-turns, and $\mathcal{R}$ is the reluctance. The reluctance of a uniform magnetic circuit can be represented by resistance-reluctance model as follows:

$$\mathcal{R} = L/(KA) \tag{3}$$

where L is the length of the circuit, K is the permeability of the material, and A is the cross-sectional area of the circuit normal to the magnetic flux. The total reluctance $\mathcal{R}$ of the whole circuit is given by the following:

$$\mathcal{R} = \mathcal{R}_{\text{core}} + 2\mathcal{R}_{\text{cover1,2}} + 2\mathcal{R}_{\text{vanex1,2}}$$
$$+ 2\mathcal{R}_{\text{vane1,2}} + \mathcal{R}_{\text{gap}} + \mathcal{R}_{\text{air}}. \tag{4}$$

Since the air gaps exist between each segment, we used $\mathcal{R}_{\text{air}}$ to present the reluctance from these air gaps. The reluctance for each segment of the vane are presented by (5)–(9), and the corresponding parts are shown in Fig. 6

$$\mathcal{R}_{\text{core}} = \frac{h_{\text{core}}}{K_{km31}S_{\text{core}}} \tag{5}$$

$$\mathcal{R}_{\text{cover1,2}} = \int_0^{r_{\text{cover}}} \frac{dr}{K_{km31}2\pi r h_{\text{cover}}} \tag{6}$$

TABLE III
DESIGNED PARAMETERS FOR BUILT-IN MRF VALVE

| Number of passages	1	Length of vane L_{vanex}	14 mm
Coil winding turns N	400	Height of vane h_{vane}	11 mm
Coil resistance	3.2 Ω	Height of passage h_{gap}	1 mm
Height of core h_{core}	23 mm	Width of passage l_{gap}	5.5 mm
Raidus of core r_{core}	14 mm	Width of vane w_{gap}	17 mm
Height of conductor h_{cover}	4 mm	Permeability of air K_0	1 μ_0
Raidus of shaft r_{cover}	30 mm	Permeability of K-m31 K_{km31}	2500μ_0
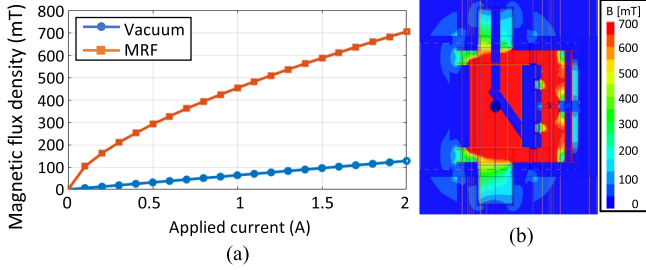
Fig. 7. Simulated results of magnetic flux density in MRF valve passage. (a) Simulation results by formulation. (b) FEM results by ANSYS.

$$\mathcal{R}_{\text{vanex}1,2} = \frac{l_{\text{vanes}}}{2KS_{\text{vanex}}} = \frac{l_{\text{vanex}}}{2K_{km31}h_{\text{cover}}w_{\text{gap}}} \quad (7)$$

$$\mathcal{R}_{\text{vane}1,2} = \frac{h_{\text{vanes}}}{KS_{\text{vane}}} = \frac{h_{\text{vane}}}{K_{km31}L_{\text{vanex}}w_{\text{gap}}} \quad (8)$$

$$\mathcal{R}_{\text{gap}} = \frac{h_{\text{gap}}}{KS_{\text{gap}}} = \frac{h_{\text{gap}}}{2K_{\text{MRF}}L_{\text{gap}}w_{\text{gap}}}. \quad (9)$$

The magnetic permeability in air K_0 is $4\pi \times 10^{-7}$ H/m, the magnetic permeability of K-M31 K_{km31} is 3.14×10^{-4} H/m, and the magnetic permeability of MRF K_{MRF} can be calculated by the following equation from datasheet [21]:

$$K_{km31} = 0.0002 \cdot H^{-0.37} \quad (10)$$

where H is the magnetic strength and it can be conducted by the following:

$$H = \frac{\mathcal{F}}{L_{\text{sum}}} = NI / (h_{\text{core}} + 2r_{\text{cover}} + 2l_{\text{vanes}} + 2h_{\text{vane}} + h_{\text{gap}}) \quad (11)$$

where L_{sum} is the total length of elective circuit.

By combining (1) and (4), the magnetic flux density at the gap can be calculated as follows:

$$B_{\text{gap}} = NI / \mathcal{R}S_{\text{gap}}. \quad (12)$$

With (12) and parameters in Table III, the magnetic flux in the MRF valve passage was calculated. As shown in Fig. 7(a), we simulated situations in MRF and vacuum, respectively. Since the permeability of vacuum is a constant, the magnetic flux density is proportional to the current. The permeability of MRF K_{MRF} nonlinearly varies with magnetic strength, i.e., current. Thus, the magnetic flux density grows fast and then becomes stable. The maximum magnetic flux density in 2 A reaches 704 mT. as shown in Fig. 7(b), the finite element method (FEM) results using ANSYS Maxwell showed that the magnetic flux in the

MRF valve passage was 675 mT at an applied current of 2 A, which consists of our simulation.

VI. TORQUE MODELING

A. Multiphysics Coupling Model

From the electromagnetic circuit modeling, the relationship between the magnetic flux and current was established. We can then use the results for torque modeling and active-drive control design. Since the flow inside the MRF valve satisfy the Poiseuille's law, based on the Hagen–Poiseuille equation, the pressure difference ΔP between the two chambers is given by the following:

$$\Delta P = \frac{128 \cdot \mu_{\text{MRF}}l_{\text{valve}}Q_A}{\pi d^4} \quad (13)$$

where μ_{MRF} is the viscosity of the MRF, l_{valve} is the length of the MRF valve, Q_A is the flowrate inside the valve, and d is the diameter of the valve. The viscosity of MRF μ_{MRF} is controlled by the magnetic field, and the relationship can be described by Bigham model [22] as follows:

$$\mu_{\text{MRF}} = \mu_{\infty} + (\mu_0 - \mu_{\infty}) \cdot 2 \cdot \left(e^{-\alpha S\mu B} - 0.5e^{-2\alpha S\mu B}\right) \quad (14)$$

where μ_0= 0.166 Pa·s, μ_{∞}= 3.8 Pa·s, and $\alpha S\mu = 4.5\text{T}^{-1}$.

Since the entrance of the MRF valve is a rectangular shape instead of a circular shape, we converted the rectangular to a circular shape with the following formula and calculated the diameter d:

$$d = 1.3 \cdot \left(\frac{(L_{\text{gap}} \cdot H_{\text{gap}})^5}{(L_{\text{gap}} + H_{\text{gap}})^2}\right)^{0.125} \quad (15)$$

where L_{gap} and H_{gap} can be found in Fig. 6 and Table III. The result of d is 2.4 mm.

To calculate flowrate Q_A, the volumetric efficiency of the pump and actuator needs to be taken into consideration. As we mentioned in Section IV, an 80 μm gap between the vane and housing exists, which will cause the flow leakage between the two chambers. Thus, the effective flowrate Q_A is given by the following:

$$Q_A = Q_p \cdot \eta_{v-p} \cdot \eta_{v-a} \cdot \frac{S_{\text{vane}}}{S_{\text{chamber}}} \quad (16)$$

where Q_p is the flowrate generated by the pump, η_{v-p} and η_{v-a} are the volumetric efficiency of the pump and MRF actuator, respectively. From the product datasheets, we found that the volumetric efficiency for both pump and the vane motor are around 40%. We here set the volumetric efficiency of the MRF actuator 40%, which is the same as the vane motor. Moreover, S_{vane} is the cross-sectional area of the vane and S_{chamber} is the cross-sectional area of the actuator chamber. By this equation, the flowrate that acts on the vane can be calculated. With (14)–(16), the pressure difference ΔP in (13) can be calculated.

Since the pressure receiving area of the vane A is constant, the torque τ_a is proportional to the pressure difference, and τ_a can be presented as follows:

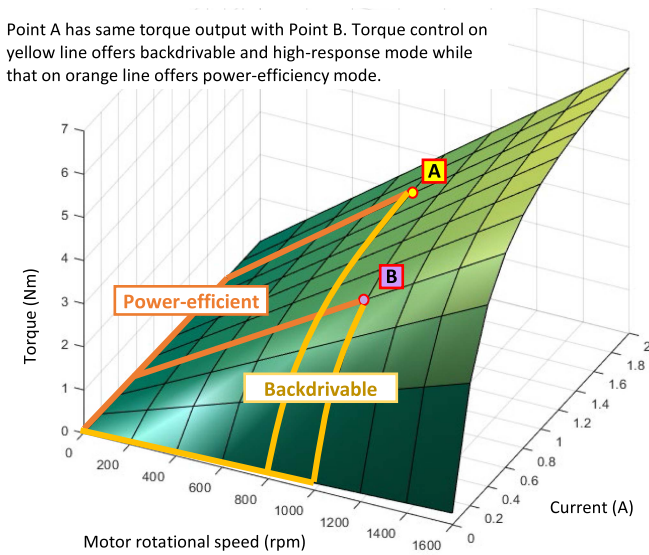$$\tau_a = \Delta P \cdot A \cdot r \quad (17)$$

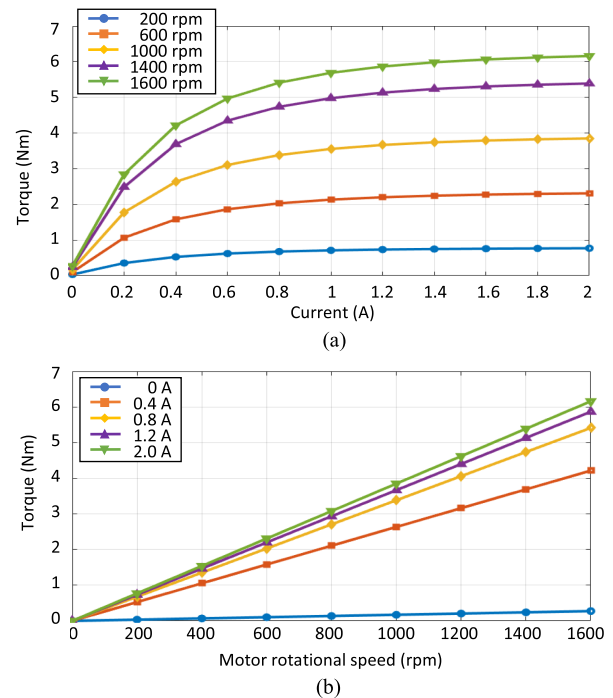Fig. 8.   Simulation results for torque by MATLAB with multi-input.

Fig. 9.   Simulation results for torque by MATLAB. (a) Simulated relationship between torque and current. (b) Simulated relationship between torque and motor speed.

where r is the radius of the vane. For the output torque τ_{out}, the mechanical efficiency needs to be considered, and the mechanical loss is mainly from friction between the sealing and shaft. By comparing calculation results and datasheet, we found that the relationship between pressure difference and output torque for this vane motor can be obtained by the following:

$$f = 3.27 \cdot \Delta P + 9.8. \tag{18}$$

Thus, the output torque τ_{out} can be calculated as follows:

$$\tau_{\text{out}} = \tau_a \cdot \eta_{m-a} = \tau_a - f \tag{19}$$

where η_{m-a} is the mechanical efficiency and f is the friction, which can be presented as (16).

By introducing the coupling model of magnetic electromagnetics (12), MRF magnetization (14), and fluid dynamics (13) into (19), the simulated torque can be calculated as shown in Figs. 8 and 9.

B. Torque Control Strategies (Multivariable Control)

As we expected, the dynamic range can be represented by a multi-input single-output system (2 inputs, 1 output) while conventional hydraulic motors only have a single-input single-output system (1 input, 1 output). Fig. 8 shows that the same torque output can be made by various combinations of the speed and current. For example, if the desired torque is around 3 N·m, we can choose the combination of a medium speed and high current (Point A) or a high speed and medium current (Point B). This is one of the most important features of the MRF actuator. Based on this feature, we can define several control modes. In Fig. 8, the yellow and orange lines represent two torque control strategies. The yellow line shows the backdrive control. The orange line shows power-efficiency control since the torque is controlled by less flowrate of the pump. Details about control modes will be introduced in Section VIII.

Fig. 9(a) and (b) show that the torque was proportional to the rotational speed and grew gradually with an increase in the current. The maximum torque for a current of up to 2 A and rotational speed of 1600 r/min was around 6.2 N·m. Evaluation experiments in Section VII will verify our model. In summary, the multiphysics coupling model we proposed could be used as a guideline for designing the structure of MRF actuator by optimizing parameters including the size of vane, MRF valve passage, and magnetic flux conductor.

VII. EVALUATION OF MRF ACTUATOR

A. Experiment Setup

We developed a test bench to compare fundamental performance of a conventional vane motor and the proposed MRF actuator (see Fig. 10). In the test bench, dc motors (FBLM86-660) drove gear pumps (Eaton MA3) to pressurize both actuators. We used rotary encoders (JT-30-340-500) and 100 N·m torque sensors (UTMI1-100Nm) to measure the speed and torque. We used pressure sensors (Parker PTDVB0251B1C2) to record the pressure. Switch power supplies of 48, 24, and 5 V were used for driving the pump, torque sensor, and encoder, respectively. An adjustable power supply was used for the built-in MRF valve to provide a variable magnetic field. To compare the conventional vane motor (in the red box of Fig. 10) and MRF actuator (in the purple box of Fig. 10), two setups were prepared. For the passive evaluation, a motor was placed after the torque sensor (red box). For the active evaluation, an arm was placed after the torque sensor (purple box).
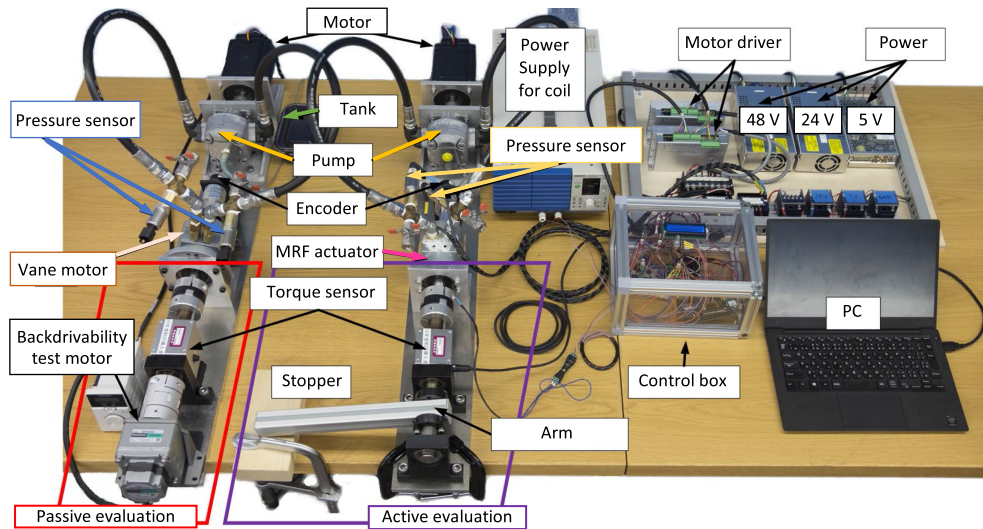
Fig. 10.   Experimental setup. Left setup is for original vane motor, and right setup is for MRF actuator. The actuators can be controlled manually by control box, or control automatically with computer.
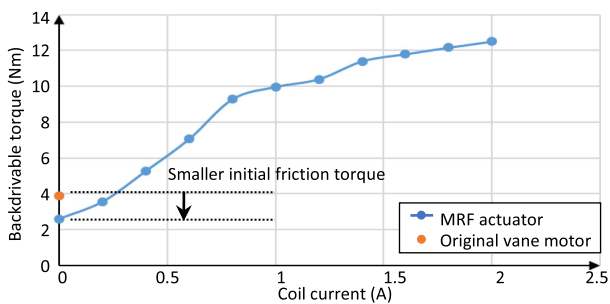

Fig. 11.   Results of friction and backdrivability test.

Fig. 12.   Results of speed test.

B. Friction and Backdrivability Test

For the passive experiment, the shaft of the MRF actuator is connected with the backdrivability test motor (BLM460S - GFV2 with gear head GFV4G50). Here, the motor rotated at a constant speed of 30 r/min, and the pump was kept without operation, and we recorded the torque value. For testing friction, no working fluid was filled into the original vane motor. The result is shown in Fig. 11. With no fluid, the initial friction of the vane motor was 3.9 N·m due to the sealing rubber.

Next, we filled both actuators with MRF 122EG. For the original vane motor, it is not backdrivable. For the MRF actuator, due to its built-in MRF valve, the fluid can freely flow from one chamber to another. Thus, it obtained good intrinsic backdrivability. When no current was applied, the initial friction of the MRF actuator was 2.6 N·m, even with the hinder of the fluid viscosity. Then, we set the current for the magnetic flux of the MRF valve passage from 0.5 to 2 A at intervals of 0.2 A. As observed in Fig. 11, with the current increase, MRF passing through the MRF valve passage solidified, so the torque required to backdrive the shaft increased up to 12.5 N·m, which was small. Compared to 8.3 N·m of the bearable startup torque of a harmonic drive gear [25], 2.6 N·m of the startup torque of
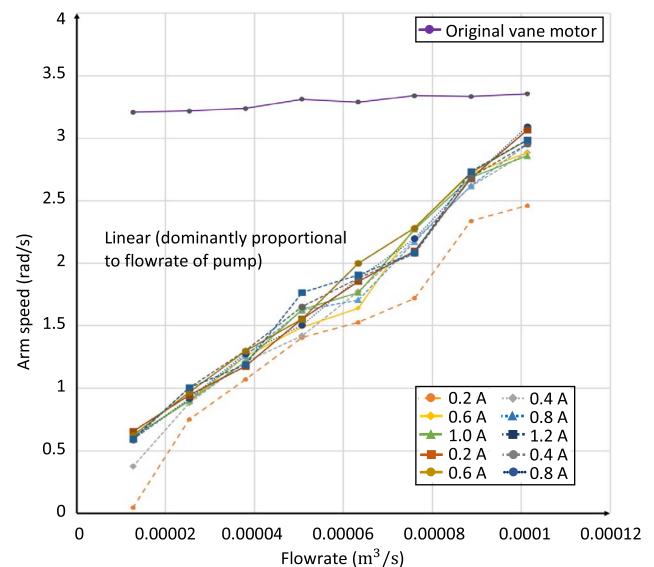
the MRF actuator was much smaller. The experimental results showed that the proposed MRF actuator had low initial friction and adjustable high intrinsic backdrivability.

C. Actuator Speed Test

In this experiment, the arm is free. By operating the motor, the pump generates various flowrates to drive actuators. We measured the speed of the arm during a motion from 0° to 90° and the results are shown in Fig. 12. The speed for both the original vane motor and MRF actuator increased linearly along with the increment of flowrate. For the MRF actuator, the speeds increased proportionally without the effect of current change. This means that the speed was dominantly determined by the
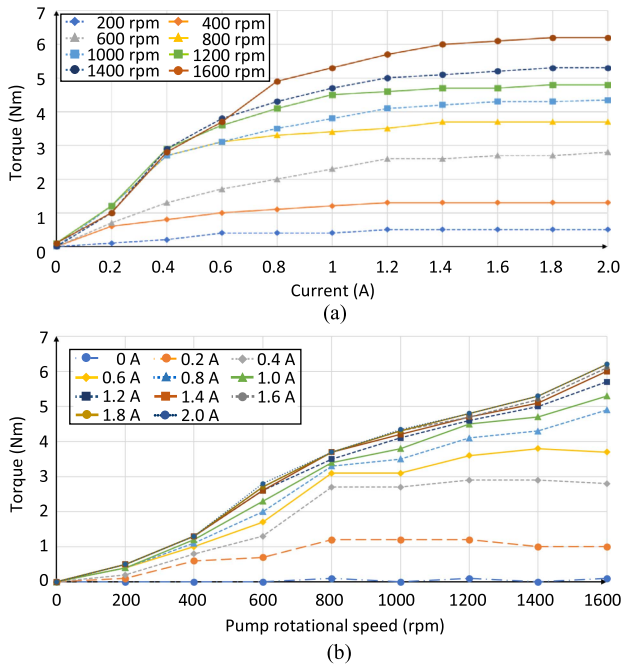
Fig. 13.   Results of torque test. (a) Torque versus current. (b) Torque versus pump speed.

Fig. 14.   Comparison between original vane motor and MRF actuator.

pump flowrate. From Fig. 11, their relationship in our setup can be represented by data fitting as follows:

$$v = 27000 \cdot u + 0.110 \cdot I - 0.3 \tag{20}$$

where v is the arm speed (rad/s), u is the flowrate (m^3/s), and I is the current (A). The coefficient of determination R^2 is around 0.8 (at 0.5 A) to 0.94 (at 0.8–2.0 A). For this equation, we can also see that the flowrate dominates the rotational speed of the actuator. Moreover, the MRF actuator had a larger speed range as compared to the original vane motor, owing to utilizing the MRF valve passage. This means that the MRF actuator could lower the drivable minimum speed, i.e., improve the low-speed controllability. The maximum speed of the MRF actuator was about 3.1 rad/s, which was close to the maximum speed of the original vane motor of 3.36 rad/s.

D. Actuator Torque Test

The output torque was tested with the arm fixed. The current was varied between 0 and 2 A at intervals of 0.2 A and the rotational speed of the pump was varied between 200 and 1600 r/min at intervals of 200 r/min. The torque–current and torque–pump speed relationships are shown in Fig. 13(a) and (b), respectively. The simulation results are consistent with experimental results. The maximum torque for both simulation and experimental results is 6.2 N·m when the pump speed is 1600 r/min and the coil is applied with 2 A. We can also draw the following conclusions.

1) Output torque could be controlled by both flowrate and current (magnetic field).

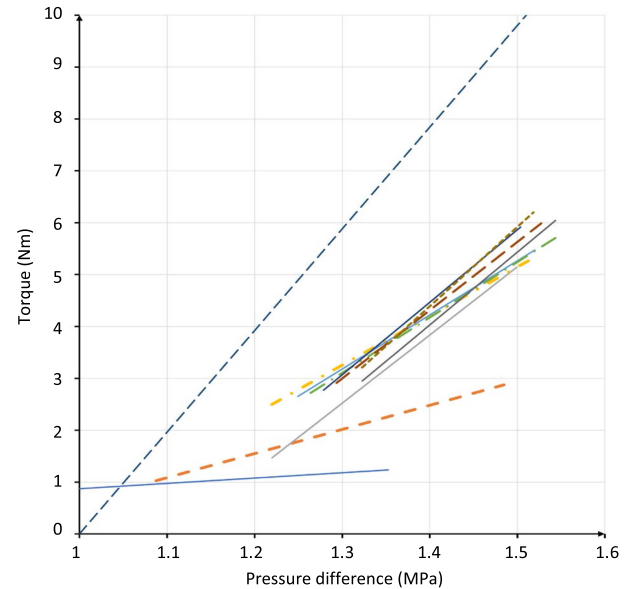2) When the current increases, the increase rate of the torque was reduced.

3) The increase in torque showed quasi-linearity when it was controlled by using the pump flowrate.

E. Comparison Between Vane Motor and MRF Actuator

Torque comparison between the original vane motor and MRF actuator is shown in Fig. 14. The torques for both actuators were measured under the same pressure difference. Just same as the vane motor, the MRF actuator showed good linearity, which led to the ease of control. As the current increased, the growth of torque became larger. From 0.6 to 2 A, the torque increased at almost the same rate. The pressure receiving area of the vane was constant and the torque was the product of the pressure difference, area, and operation radius, so the torque was the same under the same pressure, as expected in the torque simulation section. The maximum pressure and torque generated by the MRF actuator was about 1.5 MPa and about 6.2 N·m, respectively. Compared to the vane motor, the output was about half. According to (13) and (15), minimizing the height of MRF valve passage and maximizing the length of passage are expected to be an effective way to increase the output torque. In addition, applying a polytetrafluoroethylene sealing, which can help to decrease the MRF leakage with the minimum friction, would be another solution. Overall, comparing with the original vane motor, our MRF actuator had low initial friction force, high backdrivability, and better low-speed controllability. Although the torque is decreased due to sealing lack, with the method mentioned above to increase the maximum pressure, the MRF actuator is promising to generate higher output.

VIII. CONTROL SYSTEM APPLICATION

Here, we developed a multivariable active-drive controller that utilizes the features of MRF actuator. There were two manipulated variables including the pump voltage P_V for the flowrate and coil current M_A for the magnetic field. As a preliminary
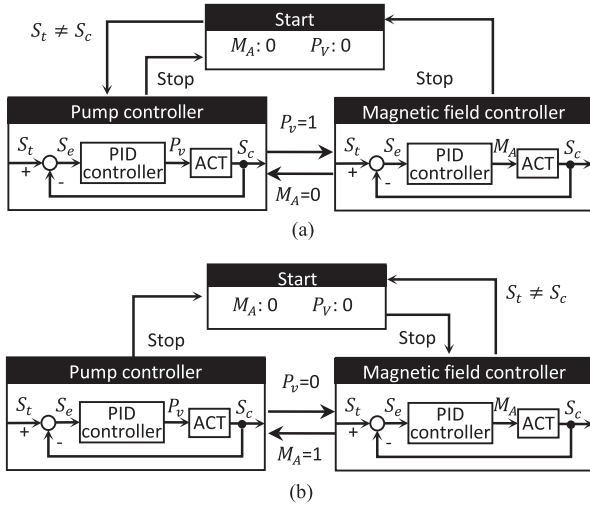
Fig. 15. Diagram of control-mode. (a) Backdrive mode (MF-save mode). (b) Power-efficient mode (pump-save mode).

evaluation, we developed several control modes using torque, speed, and backdrivability based on a state machine.

A. Control Modes

By applying the state machine and torque modeling (see Fig. 8), the system switches between the operating modes including the backdrive, power-efficiency modes. From the target speed S_t and current speed S_c, the speed error S_e in the pump control is given by $S_e = S_t - S_c$. In addition, the velocity error S_e under the magnetic field control is $S_e = (S_t - S_c)\sin(S_c \cdot P_V)$. The above modes can be realized by controlling the pump flowrate (i.e., pump voltage) and magnetic field (i.e., coil current), and an initial state different from each control mode.

1) *Backdrive mode:* The control diagram is shown in Fig. 15(a). Backdrivability largely depends on the viscosity of the MRF in the MRF valve passage. Thus, high backdrivability will be achieved by keeping the maximum flowrate with pump voltage, P_V (= 0.4 V), where the actuator does not start to rotate at M_A= 0 and changing the coil current M_A.

2) *Power-efficiency mode:* The control diagram is shown in Fig. 15(b). Compared with the electric power required to generate the magnetic field, the operating power of the pump is higher. Thus, contrary to the backdrive mode, this mode uses a large magnetic field applied M_A (= 2.0 A) and the required minimum pump voltage P_V.

B. Control Modes Experiments and Results

1) *Backdrive mode:* Fig. 16(a) shows the torque at different pump flowrates, in which the horizontal axis is the arm speed. We observed that with the rotational speed increased, the torque in the power-efficiency mode increased rapidly and then became steady. While, in the backdrive mode, the torque increased slowly and then rapidly. At the same arm speed, the torque for the
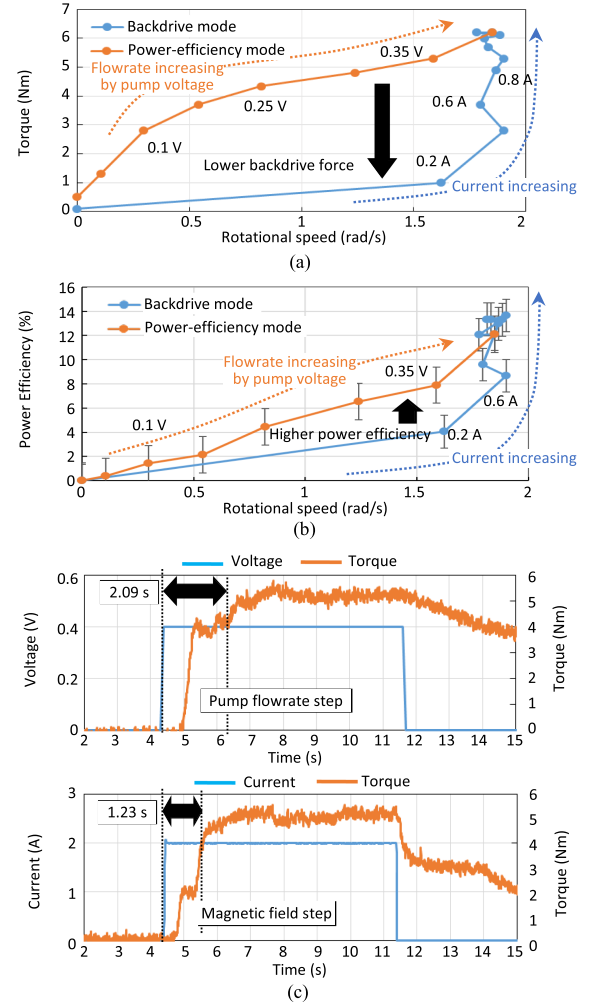

Fig. 16. Results of control experiments. (a) Backdrivability test. (b) Power-efficiency test. (c) Responsiveness evaluation.

backdrivable mode was lower than that for the power-efficiency mode, which made the robot arm easy to backdrive. The results show that this mode offered high backdrivability, which would be suitable for human-robot cooperation applications.

2) *Power-efficiency mode:* The definition of power efficiency is the ratio between output power and input power. We calculated the output power P_o by the following:

$$P_o = \tau_{\text{arm}} \cdot \omega_{\text{arm}} \tag{21}$$

where τ_{arm} and ω_{arm} are the torque and angular speed by the MRF actuator, respectively. The input power P_i can be calculated as follows:

$$P_i = V_{\text{motor}} \cdot I_{\text{motor}} + V_{\text{coil}} \cdot I_{\text{coil}} \tag{22}$$

where V_{motor} and I_{motor} are the voltage and current applied in motor, respectively, and V_{coil} and I_{coil} are the voltage and current consumed by coil for magnetic field, respectively. Thus, the power efficiency can be presented as follows:

$$P_E = \frac{P_o}{P_i} . \tag{23}$$

Different power efficiency was presented in different pump speeds, as shown in Fig. 16(b). From the figure, we found that the power efficiency in this mode was better under the same pump speed and confirmed that this mode could be achieved. This mode can be applied to long-term tasks.

3) *Responsiveness evaluation:* The responsiveness of the pump is 400 ms, while the responsiveness of the magnetic field is 20 ms. Thus, we investigated the responsiveness that is dominated by the pump or magnetic field. In the pump-dominated test, the control logic was the same as the power-efficiency mode. The coil current M_A was set to 2.0 A in advance, then we recorded the torque change while using a 0.4 V voltage step for the pump. In the magnetic field-dominated test, after pump voltage P_V set to 0.4 V, a 2 A coil current step was applied. The response time was recorded as a required time to obtain 80% of torque to the target torque ($= 5.0$ N·m). Results are shown in Fig. 16(c). The upper figure shows the pump-dominated responsiveness, and the lower figure shows the magnetic field-dominated responsiveness. From the figures, it is obvious that the response rates dominated by the magnetic field is different from that of the pump. In the pump-dominated situation, the actuation speed is mainly controlled by flowrate, which is limited by pump performance. In the magnetic field-dominated situation, the actuator is in a "pre-charged" state due to the continuous flow from the pump, after operating the built-in MRF valve with current, the actuator can exhibit faster responsiveness. Thus, different responsiveness performance appeared in the evaluation.

IX. Conclusion

In this article, we proposed a simple structure vane-type MRF rotary actuator with high output torque and controllable backdrivability and verified the feasibility of the active-drive controller. Specifically, we designed a new built-in MRF valve in the actuator and simulated output torque based on the multiphysics coupling model including electromagnetics, MRF magnetization, and fluid dynamics. The manipulated variables of the MRF actuator are pump flowrate and magnetic field, which could provide a wider dynamic range of output torque and backdrivability. We designed several control modes. From the fundamental experiments, we confirmed that the MRF actuator had low initial friction force, high backdrivability, and better low-speed controllability, compared with the original vane motor. Control modes well demonstrated the advantages of MRF actuator. We confirmed from the experiments that the proposed multiphysics modeling worked adequately and the MRF actuator possessed high output and intrinsic backdrivability. This study can contribute to creating guidelines for design and control of the MRF actuators.

Still, there are limitations to be addressed in the future. The mathematical model is required to optimize design parameters. Specifically, the built-in MRF valve needs to be optimized to increase torque output (e.g., by increasing a passage length and decreasing its area). Also, the optimization of MRF [9]

can also be applied. For example, high output can be given by MRF with higher magnetic saturation, fast responsiveness can be provided by MRF containing iron particles fabricated with strong ferromagnetic materials, and good backdrivability can be provided by MRF with a low viscosity oil medium. Moreover, for cooperative applications, an intelligent controller can be developed by introducing the machine learning scheme to understand environmental situations and select a suitable control mode.

References

[1] S. A. Bowyer and F. Rodriguez y Baena, "Dissipative control for physical human– robot interaction," *IEEE Trans. Robot.*, vol. 31, no. 6, pp. 1281–1293, Dec. 2015.

[2] O. Mendoza-Trejo and C. A. Cruz-Villar, "Robust concurrent design of a 2-DOF collaborative robot (Cobot)," *IEEE/ASME Trans. Mechatronics*, vol. 26, no. 1, pp. 347–357, Feb. 2021.

[3] A. Schmitz *et al.*, "A concept for a robot arm with adjustable series clutch actuators and passive gravity compensation for enhanced safety," in *Proc. IEEE Int. Conf. Adv. Intell. Mechatronics*, 2015, pp. 1322–1327.

[4] B. Vanderborght *et al.*, "Variable impedance actuators: A review," *Robot. Auton. Syst.*, vol. 61, no. 12, pp. 1601–1614, 2013.

[5] M. C. Sanchez-Villamañan, J. Gonzalez-Vargas, D. Torricelli, J. C. Moreno, and J. L. Pons, "Compliant lower limb exoskeletons: A comprehensive review on mechanical design principles," *J. Neuroeng. Rehabil.*, vol. 16, no. 55, pp. 1–16, 2019.

[6] K. Isik, S. He, J. Ho, and L. Sentis, "Re-engineering a high performance electrical series elastic actuator for low-cost industrial applications," *J. Actuators*, vol. 6, no. 1, pp. 1–16, 2017.

[7] R. Ham, T. G. Sugar, B. Vanderborght, K. W. Hollander, and D. Lefeber, "Compliant actuator designs," *IEEE Robot. Automat. Mag.*, vol. 16, no. 3, pp. 81–94, Sep. 2009.

[8] B. Xiao, L. Cao, S. Xu, and L. Liu, "Robust tracking control of robot manipulators with actuator faults and joint velocity measurement uncertainty," *IEEE/ASME Trans. Mechatronics*, vol. 25, no. 3, pp. 1354–1365, Jun. 2020.

[9] Y. Yao, Q. Huang, Y. Peng, and T. Oiwa, "Hybrid position, posture, force and moment control with impedance characteristics for robot manipulators," in *Proc. IEEE Int. Conf. Mechatronics Automat.*, 2011, pp. 2129–2134.

[10] W. Lee and W. K. Chung, "Disturbance-observer-based compliance control of electro-hydraulic actuators with backdrivability," *IEEE Robot. Automat. Lett.*, vol. 4, no. 2, pp. 1722–1729, Apr. 2019.

[11] P. Zhang, M. Kamezaki, K. Otsuki, Z. He, H. Sakamoto, and S. Sugano, "Development of anti-sedimentation magnetorheological fluids and its implementation to MR damper," in *Proc. IEEE/ASME Int. Conf. Adv. Intell. Mechatronics*, 2019, pp. 400–405.

[12] D. S. Walker, D. J. Thoma, and G. Niemeyer, "Variable impedance magnetorheological clutch actuator and telerobotic implementation," in *Proc. IEEE/RSJ Int. Conf. Intell. Robots Syst.*, 2009, pp. 2885–2891.

[13] Z. He, M. Kamezaki, P. Zhang, S. Shembekar, R. Tsunoda, and S. Sugano, "A prototype power transmission system with backdrivability and responsiveness using magnetorheological fluid direction converter and clutch," in *Proc. IEEE Int. Conf. Syst., Man, Cybern.*, 2020, pp. 3702–3707.

[14] J. W. Sohn, J.-S. Oh, and S.-B. Choi, "Design and novel type of a magnetorheological damper featuring piston bypass hole," *Smart Mater. Struct.*, vol. 24, pp. 1–13, 2015.

[15] G. A. Dominguez, M. Kamezaki, and S. Sugano, "Proposal and preliminary feasibility study of a novel toroidal magnetorheological piston," *IEEE/ASME Trans. Mechatronics*, vol. 22, no. 2, pp. 657–668, Apr. 2017.

[16] *General Catalog*, HarmonicDrive, Beverly, MA, US, 2007, pp. 157–176.

[17] J. Mattila, J. Koivumaki, D. G. Caldwell, and C. Semini, "A survey on control of hydraulic robotic manipulators with projection to future trends," *IEEE/ASME Trans. Mechatronics*, vol. 22, no. 2, pp. 669–680, Apr. 2017.

[18] S. Sakama, "Trend and outlook of hydraulic technology," *KYB Technol. Rev.*, vol. 56, pp. 1–5, 2018.

[19] Rexroth Bosch Group, Lohr a. Main, Germany, "Variable displacement pump A10VSO datasheet," RE 92711/01.12.

[20] H. Sahin, F. Grodaninejad, X. Wang, and Y. Liu, "Response time of magnetorheological fluids and magnetorheological valves under various flow conditions," *J. Mater. Syst. Struct.*, vol. 23, no. 9, pp. 949–957, 2012.

[21] L. T. Data, "MRF-122EG magneto-rheological fluid," *LORD Corp.*, vol. 48, pp. 1–2, 2008.

[22] G. Hu, J. Zhang, F. Zhong, and L. Yu, "Performance evaluation of an improved radial magnetorheological valve and its application in the valve controlled cylinder system," *Smart Mater. Structures*, vol. 28, pp. 1–18, 2019.

[23] P. Zhang, M. Kamezaki, K. Otsuki, Z. He, H. Sakamoto, and S. Sugano, "Development of a vacuum suction cup by applying magnetorheological elastomers for objects with flat surfaces," in *Proc. IEEE/ASME Int. Conf. Adv. Intell. Mechatronics*, 2020, pp. 777–782.

[24] M. Zubieta, S. Eceolaza, M. Elejabarrieta, and M. Bou-Ali, "Magnetorheological fluids: Characterization and modeling of magnetization," *Smart Mater. Structures*, vol. 18, 2009, Art. no. 095019.

[25] T. Ishida and A. Takanishi, "A robot actuator development with high backdrivability," in *Proc. IEEE Conf. Robot., Automat. Mechatronics*, 2006, pp. 1–6.

[26] A. Mazumdar *et al.*, "Synthetic fiber capstan drives for highly efficient, torque controlled, robotic applications," *IEEE Robot. Automat. Lett.*, vol. 2, no. 2, pp. 554–561, Apr. 2017.

Peizhi Zhang (Student Member, IEEE) received the B.S. and M.S. degrees in mechanical engineering from Waseda University, Shinjuku, Japan, in 2017, and 2019, respectively. Since September 2019, he has been working toward the Ph.D. degree in mechanical engineering as a student of the Graduate Program for Embodiment Informatics, Waseda University Program for Leading Graduate Schools, Shinjuku.

He is currently a special Researcher of the Japan Society for the Promotion of Science. His research interests include application of smart materials, and development of soft actuators and compliant actuators.

Mitsuhiro Kamezaki (Member, IEEE) received the B.S., M.S., and Dr. Eng. degrees in mechanical engineering from Waseda University, Tokyo, Japan, in 2005, 2007, and 2010, respectively.

From 2007 to 2008, he was a Visiting Research Associate in the 21st century COE Program, Waseda University. From 2008 to 2010, he was a Research Associate in the Global COE Program, Waseda University. From 2010 to 2013, he was a Research Associate with the Department of Modern Mechanical Engineering, Waseda University. He is currently an Associate Professor with the Research Institute for Science and Engineering, Waseda University. His current research interests include intelligent machine system, man-machine interface, and operator support system in operated-work machines.

Dr. Kamezaki is a member of SICE, RSJ, JSME, and the IEEE RAS. He was the recipient of the Best Paper Award from the 11th Symposium on Construction Robotics in Japan in 2008, the IROS Best Paper Award Finalist from the IEEE/RSJ IROS 2011, the SICE Young Author's Award Finalist from the 2013 SICE Annual Conference, the Young Investigation Excellence Award from RSJ in 2016, and the Best Paper Award from the IEEE/ASME AIM 2016.
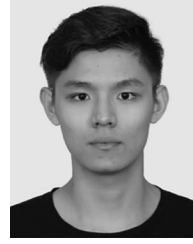
Kenshiro Otsuki received the B.S. and M.S. degrees in modern mechanical engineering from Waseda University, Tokyo, Japan, in 2017 and 2019, respectively.

His research interests include the design of MRF actuator.

Shan He received the B.S. and M.S. degrees in modern mechanical engineering from Waseda University, Tokyo, Japan, in 2016 and 2018, respectively.

His research interests include fuzzy control system.

Zhuoyi He received the B.S. and M.S. degrees in modern mechanical engineering from Waseda University, Tokyo, Japan, in 2019 and 2021, respectively.

His research interests include the design of MRF actuators and MRE soft robot.

Gonzalo Aguirre Dominguez (Student Member, IEEE) received the B.S. degree in mechatronics engineering from Monterrey Institute of Technology, Monterrey, Mexico, in 2004, and the M.S. degree in information technology and automation systems from Esslingen University of Applied Sciences, Esslingen, Germany, in 2007, and the Dr. Eng. degree in modern mechanical engineering from Waseda University, Tokyo, Japan, in 2017.

His research interests include magnetorheological fluids, development of compliant actuators, and robotic applications in physical human–robot interaction.

Shigeki Sugano (Fellow, IEEE) received the B.S., M.S., and Dr. Eng. degrees in mechanical engineering from Waseda University, Tokyo, Japan, in 1981, 1983, and 1989, respectively.

Since 1986, he has been a Faculty Member with the Department of Mechanical Engineering, Waseda University, where he is currently a Professor. Since 2014, he has served as the Dean of the School/Graduate School of Creative Science and Engineering, Waseda University. His research interests include human-symbiotic anthropomorphic robot design, dexterous and safe manipulator design, and human–robot communication.

Prof. Sugano served as the General Chair for the IEEE/ASME International Conference on Advanced Intelligent Mechatronics in 2003, and the IEEE/RSJ International Conference on Intelligent Robots and Systems in 2013. From 2001 to 2010, he served as the President of the Japan Association for Automation Advancement. He was a General Co-Chair of the 2006 IEEE/RSJ International Conference on Intelligent Robots and Systems and a Program Co-Chair of the 2009 IEEE International Conference on Robotics and Automation. He also served as the General Co-Chair of the 2012 IEEE International Conference on Robotics and Automation, the Program Chair of the 2012 IEEE/ASME International Conference on Advanced Intelligent Mechatronics. In 2017, he served as the President of SICE. He is a Fellow of four academic societies, IEEE, the Japan Society of Mechanical Engineers, the Society of Instrument and Control Engineers, and the Robotics Society of Japan.